ACADEMIC PRESS

Available online at www.sciencedirect.com
SCIENCE DIRECT®

Journal of Solid State Chemistry 174 (2003) 96–103

JOURNAL OF SOLID STATE CHEMISTRY

http://elsevier.com/locate/jssc

Synthesis and structural characterization of $Ba_{14}Pd_3Ir_8O_{33}$

Jonathan C. Burley,[a] Peter D. Battle,[a,*] Nicola A. Jordan,[a] Jeremy Sloan,[a] and François Weill[b]

[a] *Inorganic Chemistry Laboratory, University of Oxford, South Parks Road, Oxford OX1 3QR, UK*
[b] *ICMCB-CNRS, 87 Avenue du Dr. A. Schweitzer, 33608 Pessac Cedex, France*

Received 22 October 2002; received in revised form 3 February 2003; accepted 3 April 2003

Abstract

$Ba_{14}Pd_3Ir_8O_{33}$ has been prepared in polycrystalline form and characterized by X-ray, neutron and electron diffraction, lattice imaging and magnetometry. The structure can be described as the $n = 5, m = 9$ member of the $(A_3O_9)_n(A_3A'O_6)_m$ series which derives from the $n = \infty$, $m = 0$ $2H$ perovskite structure. Ir and Pd cations occupy chains of octahedral and trigonal-prismatic sites in a disordered manner. An alternative description of the structure in (3 + 1)-dimensional superspace is also presented. No magnetic phase transitions were observed above 5 K.

Keywords: Modulated structure; Hexagonal perovskite

1. Introduction

Compounds with general formula $A_wA'_xB_yO_z$ with structures related to Sr_4PtO_6 ($A = A' = Sr$) [1] have received an increasing amount of attention in recent years [2–5] because of the expectation that they will exhibit novel, one-dimensional electronic properties. The possibility of such a behavior arises because the A' and B cations are located in interstices which form chains along the [001] direction of the trigonal unit cell. These closely packed interstices lie within face-sharing O_6 polyhedra, each chain consisting of an ordered sequence of prismatic and octahedral sites; in the ideal case A' and B cations occupy the former and latter, respectively. The relatively large A cations are usually considered to occupy a second sub-lattice in the inter-chain space. Recognition of the structural similarity between these phases and the $2H$ perovskite structure enabled Darriet and Subramanian [6] to describe these structures as deriving from the hexagonal stacking of pseudo close-packed layers of stoichiometry A_3O_9 and $A_3A'O_6$, and these ideas were subsequently extended by Blake et al. [7]. Many members of this group of compounds have been shown to adopt incommensurate crystal structures and it has now been recognized [4,7] that these materials can be described as modulated composites consisting of two interacting trigonal sub-systems with a common *ab*-plane, but with different repeat distances along *z*; the (A', B)O_3 polyhedral chains constitute one subsystem, and the A cations the other. It is thus possible to analyze the structures of the materials in a (3 + 1)-dimensional (D) formalism. We have previously synthesized the phase $Ba_{14}Cu_3Ir_8O_{33}$ [7], and in this paper we describe the preparation and characterization of $Ba_{14}Pd_3Ir_8O_{33}$. The substitution of Pd^{2+} for Cu^{2+} was carried out in order to investigate the consequences for the electronic properties of having cations with relatively extensive 4*d* or 5*d* valence orbitals occupying all the sites in the polyhedral chains. We apply both the conventional supercell model and the (3 + 1)-D model to our powder diffraction data and show that the superspace formalism does indeed provide an appropriate structural description of this compound. We also describe a study of this compound by electron microscopy.

2. Experimental

A sample (ca. 3.5 g) of $Ba_{14}Pd_3Ir_8O_{33}$ was prepared using standard solid-state techniques. Stoichiometric

*Corresponding author. Fax: +44-1865-2726-90.
E-mail address: peter.battle@chem.ox.ac.uk (P.D. Battle).

0022-4596/03/$ - see front matter
doi:10.1016/S0022-4596(03)00182-8

quantities of $BaCO_3$, Ir, and Pd were thoroughly ground using an agate mortar and pestle, and subjected to the following treatment: 800°C as a powder, 68h30; at 1200°C as pellets, 71h, 43h, 49h15, 96h30, 46h, 43h, 20h40, 51h40, 70h, 17h40, 49h50, 135h15; at 1250°C as pellets, 17h20; and at 1300°C as pellets for 67h40. The progress of the reaction was followed by X-ray powder diffraction. In the earlier stages of the synthesis, the sample appeared monophasic, but the diffraction pattern could not be indexed on the basis of a commensurate primitive trigonal cell. Rather, the pattern was indexed satisfactorily using three variable unit-cell parameters a, c_1 and c_2 ($\alpha = \beta = 90°$, $\gamma = 120°$) in a manner similar to that used previously to account for incommensurate phases [2]. The sample was fired until a ratio for the two c parameters of $\frac{7}{11}$ was achieved; when the ratio c_1/c_2 is a rational fraction, the structure is commensurate and, in this case, can be described in a 14 layer supercell with $c = 11c_1 = 7c_2$. At this stage, X-ray powder diffractograms were collected over the angular range $10 \leqslant 2\theta/° \leqslant 120$, with $\Delta 2\theta = 0.02°$ and $\lambda = 1.5406$ Å ($CuK\alpha_1$) using a Siemens D5000 powder diffractometer. Neutron powder diffraction data were collected on the general materials diffractometer (GEM) at the Rutherford-Appleton Laboratories, Oxfordshire, at 290 K. The sample was contained in a 10 mm diameter vanadium can. Data were processed using the ARIEL program [8]. The highly absorbing nature of the Ir nucleus reduced the contribution to the overall neutron diffractograms from the instrument; thus subtraction of the instrumental background was performed at the 50% level. An absorption correction was also applied to the final histograms. The neutron scattering lengths and absorption cross-sections used were taken from Sears [9]; the scattering lengths used were as follows: Ba, 5.07; Ir, 10.6; Pd, 5.91; O, 5.803 fm. Full profile analysis of the supercell model was performed using the routines within the GSAS suite of programs [10]. Refinement of the (3 + 1)D model [4] against the X-ray powder profile was carried out using the JANA2000 [11] package. It has not been possible to carry out a full profile analysis of the room temperature time-of-flight neutron diffraction data using the (3 + 1)D approach because of limitations in the available software.

Electron diffraction patterns and high-resolution lattice images were collected on a JEOL 4000 EX transmission electron microscope ($C_s = 1.0$ mm; point resolution = 1.6 Å) operated at 400 kV. Images were recorded close to ideal Scherzer defocus conditions. Image simulations were performed using the unit cell refined from room temperature neutron powder diffraction data and standard multislice algorithms available within the EMS package [12]. Magnetic measurements were performed over the temperature range $5 \leqslant T/K \leqslant 300$ using a Quantum Design MPMS DC SQUID magnetometer in applied fields of 100 and 1000 Oe after cooling in both zero field (ZFC) and the applied measuring field (FC). A simple conductivity study was performed using two contact geometry; the compound is an insulator.

3. Results

3.1. X-ray and neutron diffraction

3.1.1. The supercell model

Blake et al. [7] when analyzing $Ba_{14}Cu_3Ir_8O_{33}$, imposed four constraints on the system in developing trigonal, supercell models: (i) in any one chain, trigonal-prismatic sites are always separated by at least one octahedral site; (ii) no layer has more than one-third of the oxide ions absent; (iii) the transition-metal chains at $(\frac{1}{3}, \frac{2}{3}, z)$ and $(\frac{2}{3}, \frac{1}{3}, z)$ are translated by equal and opposite amounts with respect to the chain at (0, 0, z); and (iv) the composition of the transition-metal chains is fixed, and the same oligomers formed by face-sharing transition-metal octahedra occur with the same repeat pattern in all three chains. These four assumptions limited the number of available models to three for phases of stoichiometry $Ba_{14}Pd_3Ir_8O_{33}$, all of which have the ideal space group $P321$. Of these constraints, the first two are based on observed chemical preferences, and the third and fourth were imposed to limit the number of available models. Relaxing the third constraint allows a large increase in the number of available models (estimated at a total of ca. 40), and relaxing the fourth constraint increases the number of models to well in excess of 200. Three space groups are available to these ca. 200 models. Three trial models, designated A, B, and C, were chosen for comparison with the data in this work. In model A assumptions (iii) and (iv) are relaxed, in model B assumption (iii) is relaxed, and model C conforms to the assumptions made by Blake et al. The trial models were derived by considering an idealized mixed hexagonal pseudo-close-packed stacking of Ba_3O_9 and Ba_3PdO_6 layers as described above. The models, all of which all contain 42 independent atomic sites, are shown in Fig. 1.

Attempts were made to refine each model by analyzing simultaneously one X-ray and four neutron powder diffractograms, together covering the d-spacing range $0.3 \leqslant d/Å \leqslant 15$. All models refined to give similar goodness-of-fit indicators (Table 1), with 151 variables refined in each model. The atomic displacement parameters of all ions except Pd refined to negative values in all three trial refinements; the observed negative values are likely to be an indication of the strongly absorbing nature of the sample, and the larger value for Pd may indicate a space group incoherent displacement of Pd^{2+} away from the center of the trigonal prism towards one

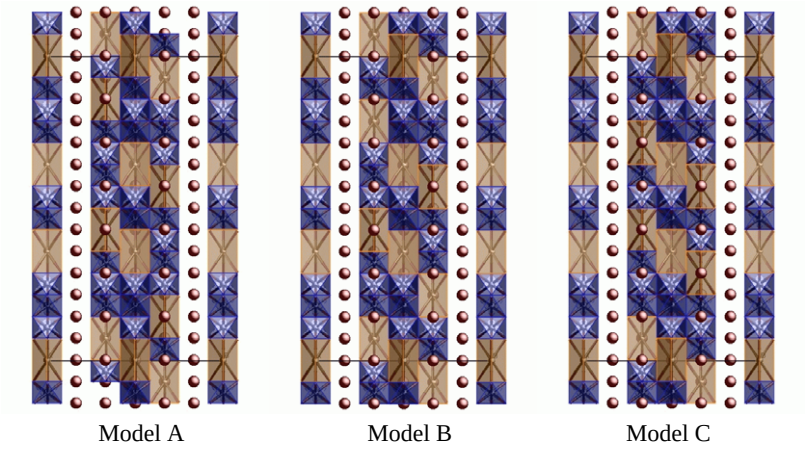

Fig. 1. Structural models A, B, and C for $Ba_{14}Pd_3Ir_8O_{33}$. Trigonal prisms are lightly shaded, octahedra are darker.

Table 1
Results of Rietveld analysis of the three test models against X-ray and neutron powder diffraction data

Model	R_{wp} (%)	R_p (%)	χ^2	DW-d	Number of variables
A	4.01	14.28	2.035	0.732	151
B	3.97	15.24	1.999	0.776	151
C	4.03	14.37	2.051	0.727	151

of the rectangular faces. Consideration of the refined bond lengths led to the rejection at this stage of models A and B. The refined bond lengths of model C were more sensible, with the Ir–O bond distances ranging between 1.65(5) and 2.54(5) Å (mean = 2.13 Å), and Pd–O distances ranging from 1.98(9) to 2.90(8) Å (mean = 2.36 Å). Whilst these extreme distances are unlikely to be correct, the median values of 2.05 and 2.39 Å, respectively, are reasonable, and compare with Ir–O distances of 1.96 and 1.99 Å in IrO_2, and a Pd–O distance of 2.19 Å (for four coordinate Pd) in PdO [13,14]. The reliable determination of structural parameters in a refinement of this complexity is clearly problematic, even with the availability of five data sets. A trial refinement in which the Pd^{2+} ions were allowed to move towards the faces of the trigonal-prismatic sites in a disordered manner was not stable. A further trial refinement was performed in which occupational disorder was introduced between the Pd^{2+} in the trigonal-prismatic sites, and the Ir^{4+} ions in the neighboring octahedra. Atomic displacement parameters and positions were fixed at the previously refined values. The Pd^{2+}:Ir^{4+} ratio in the prismatic site refined to 0.69:0.31(2); the resultant goodness-of-fit parameters were $\chi^2 = 1.949$, $R_{wp} = 3.94\%$, $R_p = 14.35\%$. Further refinement of atomic positions and displacement parameters was not possible. We thus conclude that, of our three trial models A and B are ruled out, but C is a plausible supercell structure for $Ba_{14}Pd_3Ir_8O_{33}$, provided that cation disorder is introduced into the [001] polyhedral chains. The refined atomic coordinates, resulting from the combined analysis of neutron and X-ray data, are presented in Table 2, and the results of the neutron profile analysis are shown in Fig. 2.

3.1.2. (3+1)D model

Using the (3+1)D formalism described elsewhere [4,15] significantly fewer parameters are required to describe fully the structure. The family of compounds $A_{1+x}A'_xB_{1-x}O_3$ where $Ba_{14}Pd_3Ir_8O_{33}$ corresponds to $x = \frac{3}{11}$ can be treated as modulated composite structures consisting of two interacting subsystems, $[(A', B)O_3]$ and $[A]$. In accordance with previous studies on single crystals of related systems [16–19], the superspace group $R\bar{3}m(00\gamma)0s$ was employed with the [(Pd, Ir)O_3] subsystem as the reference system. The composition and modulation vector ($\boldsymbol{q} = \gamma \boldsymbol{c}^*$) are intrinsically linked through the relationship $\gamma = (1 + x)/2$. The two subsystems are related by the application of the transformation matrices

$$W^1 = \begin{pmatrix} 1 & 0 & 0 & 0 \\ 0 & 1 & 0 & 0 \\ 0 & 0 & 1 & 0 \\ 0 & 0 & 0 & 1 \end{pmatrix}, \quad W^2 = \begin{pmatrix} 1 & 0 & 0 & 0 \\ 0 & 1 & 0 & 0 \\ 0 & 0 & 0 & 1 \\ 0 & 0 & 1 & 0 \end{pmatrix}.$$

In this superspace group a single oxygen position is required to generate all the sites in the cell and this, together with the use of Crenel functions of suitable center and width ($x_4 = \frac{1}{4}, \Delta = \frac{1}{2}$, respectively [4]) defines the sequence of octahedra and trigonal prisms in real space. In order to distinguish between the heights of the octahedra and prisms, a displacive z-modulation must be introduced; the simplest function compatible with this and the Crenel-like occupational variation is a sawtooth function. A single additional parameter, δ_O, corresponding to the maximum amplitude of the sawtooth function must be introduced. The maximum amplitudes of the sawtooth functions for all the other

Table 2
Atomic coordinates of $Ba_{14}Pd_3Ir_8O_{33}$

Atom	Position	x	y	z
Ba1	3*e*	0.647(5)	0	0
Ba2	6*g*	0.323(3)	0.990(3)	0.0692(8)
Ba3	6*g*	0.008(4)	0.681(4)	0.146(1)
Ba4	6*g*	0.988(4)	0.318(4)	0.213(1)
Ba5	6*g*	0.002(4)	0.654(4)	0.285(1)
Ba6	6*g*	0.352(3)	0.000(4)	0.358(1)
Ba7	6*g*	0.006(3)	0.676(4)	0.4318(8)
Ba8	3*f*	0	0.331(4)	1/2
Ir1	2*d*	1/3	2/3	0.116(1)
Ir2	2*d*	1/3	2/3	0.390(1)
Ir3	2*c*	0	0	0.455(1)
Ir4	2*d*	1/3	2/3	0.478(1)
Ir5	2*d*	2/3	1/3	0.334(1)
Ir6	2*c*	0	0	0.096(1)
Ir7	2*c*	0	0	0.181(1)
Ir8	2*d*	1/3	2/3	0.032(1)
Ir9	2*d*	2/3	1/3	0.156(1)
Ir10	2*c*	0	0	0.266(1)
Ir11	2*d*	1/3	2/3	0.208(1)
Ir12	2*d*	2/3	1/3	0.245(1)
O1	6*g*	0.514(8)	0.179(7)	0.016(2)
O2	6*g*	0.483(9)	0.679(8)	0.155(1)
O3	6*g*	0.853(9)	0.852(7)	0.307(2)
O4	6*g*	0.482(8)	0.814(9)	0.350(2)
O5	6*g*	0.690(8)	0.165(9)	0.371(2)
O6	6*g*	0.484(8)	0.672(9)	0.435(3)
O7	6g	0.821(8)	0.840(9)	0.415(2)
O8	6*g*	0.833(7)	0.469(8)	0.478(2)
O9	3*f*	0.16(1)	0.16(1)	$\frac{1}{2}$
O10	6*g*	0.847(9)	0.015(8)	0.059(2)
O11	6*g*	0.783(6)	0.814(6)	0.144(2)
O12	6*g*	0.336(9)	0.51(1)	0.076(2)
O13	6*g*	0.500(6)	0.172(7)	0.123(2)
O14	6*g*	0.801(6)	0.964(9)	0.216(2)
O15	6*g*	0.481(7)	0.827(6)	0.223(1)
O16	6*g*	0.642(8)	0.168(8)	0.203(2)
O17	6*g*	0.509(8)	0.186(8)	0.287(2)
Pd1	1*a*	0	0	0
Pd2	2*d*	2/3	1/3	0.055(2)
Pd3	2*d*	1/3	2/3	0.3100(9)
Pd4	2*d*	0	0	0.358(3)
Pd5	2*d*	1/3	2/3	0.572(4)

$a = b = 10.139829(9)$ Å, $c = 30.2178(4)$ Å.

atoms can be related to this one variable through simple geometrical considerations [4]. The two polyhedral cations (Pd^{2+}, Ir^{4+}) are also described by a single average position together with appropriate sawtooth functions; the widths are given by $\Delta_{Pd} = \gamma - \frac{1}{2}$ and $\Delta_{Ir} = 1 - \gamma$, the centers by $x_{4,Pd} = 0.25$ and $x_{4,Ir} = 0$ and the maximum amplitudes by $\delta_{Pd} = x\delta_O$ and $\delta_{Ir} = (1-x)\delta_O$ [4].

The Ba^{2+} cations which reside between the chains of polyhedra, lie in the second, primitive subsystem at $(\sim\frac{1}{3}, 0, \frac{1}{4})$. Two distinct Ba sites can be identified corresponding to cations which occupy either the Ba_3O_9 or the Ba_3PdO_6 layers. Again their occupational and displacive modulations can be modelled by using

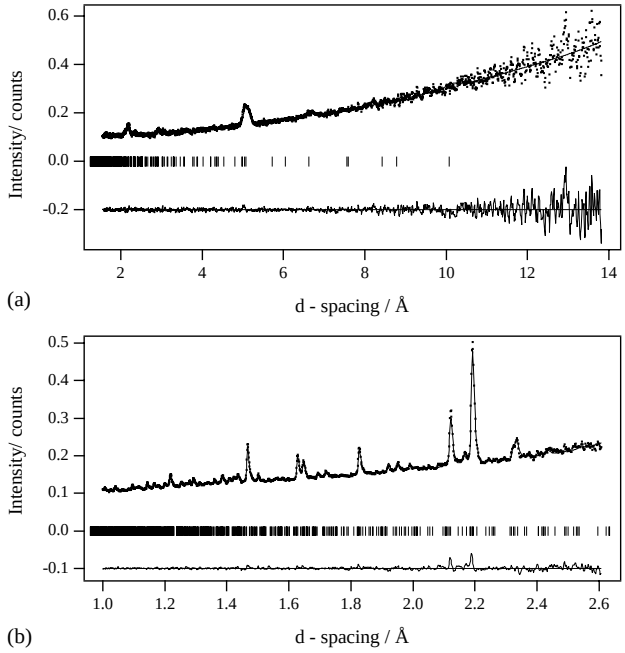

Fig. 2. Observed (■), calculated (—). and difference neutron powder diffraction profiles of $Ba_{14}Pd_3Ir_8O_{33}$. Allowed reflections are indicated by vertical lines. (a) 19.7° detector bank and (b) 90° bank.

sawtooth functions; here the widths are given by $\Delta_{Ba_1} = (1-2x)/3(1+x)$ and $\Delta_{Ba_2} = x/1+x$, the centers by $x_{4,Ba1} = 0.5$ and $x_{4,Ba2} = 0$ and the maximum amplitudes by $\delta_{Ba_1} = ((1-2x)/3x)\delta_{Ba_2}$ and $\delta_{Ba_2} = (-x/4)(1-2|\delta_O|(1-x))$ [4].

Refinement of the model against the X-ray diffraction pattern proceeded allowing a total of only 21 parameters to vary. The modulation vector component, γ, refined to a value of 0.63665(3), very close to the ideal value for the commensurate supercell ($\frac{7}{11} = 0.63636$). The isotropic temperature factors for the octahedral cation and the oxygen position refined to a negative value within one standard deviation of zero. These were subsequently set to zero and held fixed. The fraction of Pd:Ir in the prismatic and octahedral sites was allowed to vary and refined to give a Pd:Ir ratio of 0.60:0.40(5) for the prismatic site. This is in reasonable agreement with the value obtained from the 3D supercell approach. Despite a high value for the isotropic atomic displacement factor, no evidence for the displacement of Pd towards the faces of the prism was observed in difference Fourier maps.

The resultant goodness-of-fit parameters for the refinement were $\chi^2 = 1.93$, $R_{wp} = 17.06\%$, $R_p = 13.35\%$. The refined atomic coordinates are presented in Tables 3 and 4, and the results of the profile analysis in Fig. 3. The agreement between the observed and calculated profiles is very similar to that obtained for the Model C supercell consideration of both neutron and X-ray data with the occupational disorder across the octahedral and prismatic sites (where the corresponding

Table 3
Atomic coordinates of $Ba_{14}Pd_3Ir_8O_{33}$, from refinement of X-ray data set using the (3+1)D approach

Atom	x	y	z	U_{iso}/Å^2
Subsystem 1: $R\bar{3}m(00\gamma)0s$				
Pd	0	0	0	0.15(2)
Ir	0	0	0	0
O	0.167(2)	0.167(2)	1/2	0
Subsystem 2: $P\bar{3}c1\left(00\frac{1}{\gamma}\right)$				
Ba_1	0.330(2)	0	1/4	0.005(6)
Ba_2	0.350(1)	0	1/4	0.003(4)

$a = b = 10.1409(3)$ Å, $c = 2.7480(1)$ Å, $\gamma = 0.63665(3)$.

Table 4
Sawtooth parameters for $Ba_{14}Pd_3Ir_8O_{33}$, from refinement of X-ray data set using the (3+1)D approach

Atom	x_4	Δ	Amplitude
Subsystem 1: $R\bar{3}m(00\gamma)0s$			
Pd	1/4	0.13665(3)	−0.030(1)
Ir	0	0.36335(4)	−0.079(4)
O	1/4	1/2	−0.109(7)
Subsystem 2: $P\bar{3}c1\left(00\frac{1}{\gamma}\right)$			
Ba_1	1/2	0.11906	−0.0274(6)
Ba_2	0	0.2142	−0.049(2)

R-factors of the X-ray histogram refined to values of $R_{wp} = 18.69\%$, $R_p = 14.66\%$). The bond lengths from this (3+1)D approach refined to Ir–O 2.13(2) Å, Pd–O 2.32(1) Å and are in excellent agreement with the mean values obtained from the consideration of both the neutron and X-ray diffractograms in the 3D model. However, the introduction of the fourth dimension eliminated the chemically nonsensical values derived for some of the individual bond lengths in the 3D model. Additional harmonics can be introduced to model the modulations of the atoms in both the z-direction and in the xy-plane. Introduction of this additional freedom for the cations did not greatly improve the quality of the fit ($\chi^2 = 1.86$, $R_{wp} = 16.72\%$, $R_p = 13.05\%$). It proved impossible to refine significant second-order harmonics for the weakly scattering oxide ions.

3.2. Electron microscopy

Electron diffraction patterns were collected from crystallites aligned along two zone axes. The first of these is the [010] axis and the diffraction pattern is shown in Fig. 4(a). The diffraction pattern can be indexed on the basis of a commensurate 14-layer model. An alternative indexing scheme using a (3+1)D model could be employed [20,21], in which case the 0 0 5, 0 0 9, 0 0 14, and 1 0 11 reflections (Fig. 4a) would index as 0 0 3 $\bar{4}$, 0 0 $\bar{3}$ 6, 0 0 0 2, and 1 0 1 0, respectively. The pattern is modulated in the $[\bar{1}03]^*$ direction as indicated in Fig. 4(a). The selected area electron diffraction pattern collected from a crystallite aligned along the $[1\bar{1}0]$ zone axis is shown in Fig. 4(b). The 0 0 2, 0 0 5, 0 0 7, 0 0 9, 0 0 12 and 0 0 14 (most intense) reflections are clearly visible. This is again in accord with our proposed structural models based on a mixed stacking of $9 \times Ba_3PdO_6$ and $5 \times Ba_3O_9$ layers. Simulated diffraction patterns based on our three test models do not show significant differences and, with the three test models possessing the same space group $P321$, we are unable to determine which best describes our electron diffraction data.

A high-resolution lattice image collected from a crystallite aligned along the [010] zone axis is shown in Fig. 5(d), with Fig. 5(a) showing the idealized structural model, and Fig. 5(b) showing a simulation based on the results of the combined X-ray and neutron refinement with fully ordered Pd^{2+} and Ir^{4+}. Based on the information provided by the simulations, the transition-metal ions are resolved as darker areas. The features running diagonally across the image (arrows) correspond to areas of relatively low electron density; comparison with the simulated images based on the structure (model C) derived from Rietveld analysis of the powder diffraction data and the idealized structure initially suggested that these diagonal features correspond to the trigonal-prismatic sites. Comparison of the observed image with a simulation based on a model with complete ordering of Pd^{2+} and Ir^{4+} within the polyhedral chains suggested the presence of some occupational disordering between the trigonal-prismatic and octahedral sites. A model based upon the Rietveld refinement described above in which disordering was allowed lead to a greatly improved simulation of the observed data (Fig. 5(c)), and thus a description of $Ba_{14}Pd_3Ir_8O_{33}$ in which the Ir^{4+} and Pd^{2+} ions are partially disordered over the six coordinate polyhedral sites is preferred. In particular, the diagonal intensity distribution in the image is far better described using the disordered model and we therefore take it to be sensitive to the distribution of Pd^{2+} cations, rather than to the distribution of prismatic sites. We conclude this discussion of the [010] projection image by remarking that the image is in excellent agreement with a cation-disordered model C and hence with the X-ray and neutron powder diffraction studies presented earlier; the imaging of the Pd^{2+} ions is particularly noteworthy.

3.3. Magnetometry

The variation of the inverse molar magnetic susceptibility of $Ba_{14}Pd_3Ir_8O_{33}$ with temperature is shown in Fig. 6. The ZFC and FC data sets overlie within

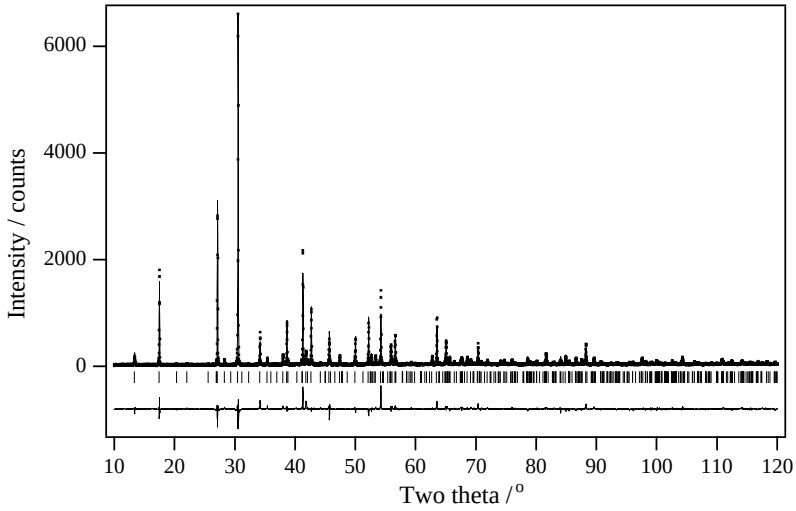

Fig. 3. Observed (■), calculated (—), and difference profiles from (3 + 1)D Rietveld refinement of X-ray powder diffraction data. Allowed reflections are indicated by vertical lines.

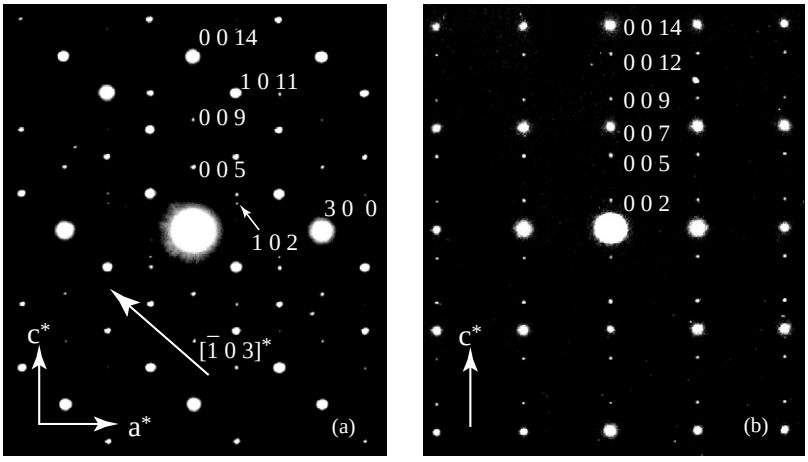

Fig. 4. (a) [010] and (b) $[1\bar{1}0]$ selected area electron diffraction patterns for $Ba_{14}Pd_3Ir_8O_{33}$. The $[\bar{1}03]$ direction of the intensity modulation is indicated by an arrow.

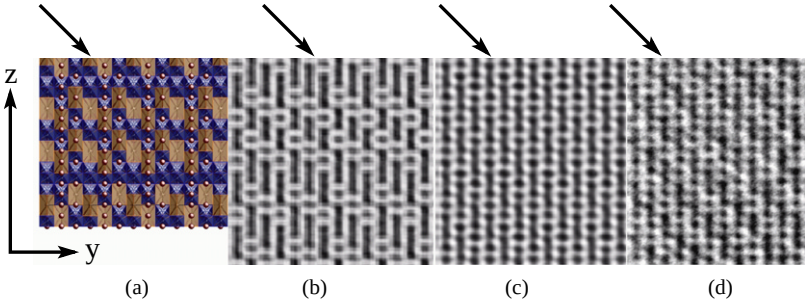

Fig. 5. (a) Ideal structure of $Ba_{14}Pd_3Ir_8O_{33}$, model C, [100]; (b) simulated image calculated for crystal thickness of 20 Å and 40 nm defocus; (c) simulated image with Pd/Ir disorder; and (d) observed image.

experimental error. No transitions are apparent in the data collected, which could be fitted over the entire temperature range ($5 \leqslant T/K \leqslant 300$) to the Curie–Weiss law, modified to include a temperature-independent term (α). Numerical values pertaining to the fits in fields of 100 and 1000 Oe are given in Table 5; the susceptibility shows no significant field dependence.

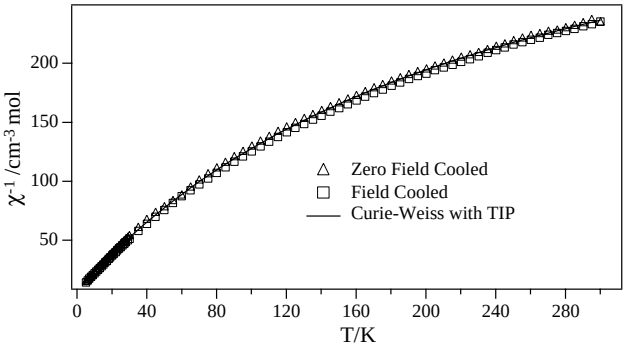

Fig. 6. Temperature dependence of the inverse molar magnetic susceptibility of $Ba_{14}Pd_3Ir_8O_{33}$ measured in an applied field of 100 Oe.

Table 5
Magnetic parameters for $Ba_{14}Pd_3Ir_8O_{33}$

H/Oe	C (cm^3 K mol^{-1})	θ (K)	$\alpha/10^{-3}$ (cm^3 mol^{-1})
100	0.565(7)	−3.7(1)	2.4(1)
1000	0.61(1)	−3.7(2)	2.1(1)

4. Discussion

The combined use of X-ray, neutron, and electron diffraction, coupled with HRTEM imaging, has allowed a full structural characterization of $Ba_{14}Pd_3Ir_8O_{33}$. The application of HRTEM imaging was particularly important, allowing confirmation of the occupational disordering within the polyhedral chains suggested by the combined X-ray and neutron refinement. The number of available variables in the refinement of the supercell was problematic, even using four neutron diffractograms and one X-ray diffractogram in a combined refinement, and did not allow us to determine whether the Pd^{2+} ions were displaced within the trigonal-prismatic sites, as has been observed previously with Cu^{2+} [2,22]. The successful application of the superspace model allowed significantly fewer parameters to be specified to describe the structure and confirmed the value of the modulation vector to be very close to the ideal commensurate value. Further support for the disordering across the Pd/Ir sites was evident from this alternative analysis of the X-ray diffraction data. The importance of occupational disorder between Pd^{2+} and Ir^{4+} was clearly apparent in the high-resolution image, which is consistent with the Rietveld analyses. This disordering has been reported previously from powder diffraction data in the $Ba_6CuMn_4O_{15}$ and $Ba_6CuIr_4O_{15}$ [2,7] but has not previously been observed in direct space.

The measured effective magnetic moment of the Ir^{4+} cation (0.627 μ_B) is significantly lower than the minimum value expected for a low-spin d^5 cation (1.73 μ_B). This reduction is likely to reflect short-range spin pairing within the polyhedral chains. Unlike in $Ba_6CuMn_4O_{15}$, but as in $Ba_6CuIr_4O_{15}$, no transition indicating the onset of magnetic ordering, either one or three dimensional, was observed. The lack of magnetic ordering is likely to be a result of the disordering of the transition-metal ions over the polyhedral sites.

5. Conclusion

A monophasic, commensurate, sample of $Ba_{14}Pd_3Ir_8O_{33}$ has been characterized by X-ray, neutron and electron diffraction, high-resolution electron microscopy, magnetometry, and conductivity studies, which have shown that the sample prepared can be considered to possess a structure comprising of $9 \times Ba_3PdO_6$ and $5 \times Ba_3O_9$ layers stacked in a pseudo-close-packed manner or, alternatively, as a modulated composite structure consisting of two interacting subsystems. The stacking sequence of these layers has been deduced through use of HRTEM, coupled with electron, X-ray, and neutron diffraction studies. The presence of extensive occupational disorder was indicated by X-ray and neutron powder diffraction, and confirmed by high-resolution electron microscopy. This is the first example of a compound in this structural family containing mixed $4d/5d$ ions in the polyhedral chains although the degree of orbital overlap was not large enough to lead to metallic conductivity. The introduction of Pd^{2+} into the trigonal-prismatic sites did not lead to a long-range structural distortion, thus interactions between transition-metal ions were frustrated and a long-range-ordered magnetic ground state was not stable. The disordering of octahedra:prism occupation along z is likely to reinforce this instability.

Acknowledgments

We thank V. Petricek and M. Dusek for allowing us to access test versions of JANA2000. We are grateful to the EPSRC, the Royal Society and the British Council for financial support and to J. Darriet, S. van Smaalen and M.Wünschel for stimulating discussions.

References

[1] J.J. Randall, L. Katz, Acta Crystallogr. 12 (1959) 519–521.
[2] E.J. Cussen, J.F. Vente, P.D. Battle, J. Am. Chem. Soc. 121 (1999) 3958–3967.
[3] K. Boulahya, M. Parras, J.M. González-Calbet, J. Solid State Chem. 142 (1999) 419–427.
[4] J.M. Perez-Mato, M. Zakhour-Nakhl, F. Weill, J. Darriet, J. Mater. Chem. 9 (1999) 2795–2808.

[5] C.A. Moore, E.J. Cussen, P.D. Battle, J. Solid State Chem. 153 (2000) 254–262.
[6] J. Darriet, M.A. Subramanian, J. Mater. Chem. 5 (1995) 543–552.
[7] G.R. Blake, P.D. Battle, J. Sloan, J.F. Vente, J. Darriet, F. Weill, Chem. Mater. 11 (1999) 1551–1558.
[8] P.G. Radaelli, www.isis.rl.ac.uk/disordered/gem/gem.
[9] V.F. Sears, Neutron News 3 (1992) 26–37.
[10] A.C. Larson, R.B. Von Dreele, General Structure Analysis System (GSAS), Technical Report LAUR 86-748, Los Alamos National Laboratory, 1990.
[11] V. Petricek, M. Dusek, The Crystallographic Computing System JANA2000, Technical Report, Institute of Physics, Praha, Czech Republic, 2000.
[12] P.A. Stadelmann, Ultramicroscopy 21 (1987) 131–145.
[13] A.A. Bolzan, C. Fong, B.J. Kennedy, C.J. Howard, Acta Crystallogr. B 53 (1997) 373–380.
[14] O. Glemser, G. Peuschel, Z. Anorg. Allg. Chem. 281 (1955) 44–53.
[15] S. van Smaalen, Crystal Rev. 4 (1995) 79–202.
[16] M. Zakhour-Nakhl, J.B. Claridge, J. Darriet, F. Weill, H.C. zur Loye, J.M. Perez-Mato, J. Am. Chem. Soc. 122 (2000) 1618–1623.
[17] M. Zakhour-Nakhl, F. Weill, J. Darriet, J.M. Perez-Mato, Int. J. Inorg. Mater. 2 (2000) 71–79.
[18] M. Zakhour-Nakhl, J. Darriet, J.B. Claridge, H.C. zur Loye, F. Weill, J.M. Perez-Mato, Int. J. Inorg. Mater. 2 (2000) 503–512.
[19] K.E. Stitzer, A.E. Abed, J. Darriet, H.C. zur Loye, J. Am. Chem. Soc. 123 (2001) 8790–8796.
[20] P.D. Battle, G.R. Blake, J. Darriet, J.G. Gore, F. Weill, J. Mater. Chem. 7 (1997) 1559–1564.
[21] M. Onoda, M. Saeki, A. Yamamoto, K. Kato, Acta Crystallogr. B 49 (1997) 929–936.
[22] M. Neubacher, H. Müller-Buschbaum, Z. Anorg. Allg. Chem. 607 (1992) 124–127.